Journal of Magnetic Resonance 206 (2010) 264–268

Contents lists available at ScienceDirect

Journal of Magnetic Resonance

journal homepage: www.elsevier.com/locate/jmr

Communication

# Contrast STRAFI–MAS imaging

Alan Wong, Dimitris Sakellariou *

*CEA, DSM, IRAMIS, SIS2M, Laboratoire Structure et Dynamique par Résonance Magnétique, F-91191 Gif-sur-Yvette, France; UMR CEA/CNRS no 3299 – SIS2M, France*

ARTICLE INFO

*Article history:*
Received 20 May 2010
Revised 2 July 2010
Available online 31 July 2010

*Keywords:*
Stray-field
Magic-angle spinning
Sample rotation
Contrast imaging
MRI

ABSTRACT

We demonstrate the possibility of multidimensional contrast ($T_1$-, $T_2$-weighted and triple-quantum filtered) magnetic resonance imaging using a simple and effective solid-state NMR technique, stray-field imaging with sample magic-angle spinning (STRAFI–MAS). This imaging technique can be easily implemented in today's standard solid-state NMR laboratory, making it a potentially valuable imaging application to material science.



## 1. Introduction

Despite the power of computed tomography (CT) to provides good spatial image resolution [1] (ability to distinguish two structures with small distance apart), magnetic resonance imaging (MRI) is still far superior technique over CT in contrast resolution (ability to distinguish the differences between two similar but different media, such as water *vs* lipid molecules, healthy *vs* unhealthy tissue, and soft tissue *vs* hard rigid material) [2,3]. Moreover, MRI is also a non-hazardous imaging technique, giving an advantageous over CT [4]. The principle of contrast MRI is based on the fact that protons in different media give rise to different signal intensity regulated by the spin properties, such as longitudinal ($T_1$) and transverse ($T_2$) relaxation [2,3]. Today, a vast library of MRI pulse sequences [5] is available in modern medical hardware to manipulate the signal intensity based on the individual spin property, including $T_1$- or $T_2$-weighted images. Thereby, contrast MRI is commonly used as a diagnostic tool in medicine for the *in vivo* visualization of the structure and physiology of humans or animals [6,7].

Recently Baltisberger et al. [8] have introduced a new MRI technique for solid materials that does not rely on the use of complex imaging equipment such as pulsed-field gradient (PFG). The technique is simple, and can be easily implemented in the modern NMR facilities. It only requires a standard NMR magnet for the free accessible stray-field gradient (a single $z$-directional $G_z$), a conventional magic-angle spinning (MAS) probe and its pneumatic controller, and a series of MAS synchronization radio-frequency (rf) pulses in the pulse sequence. The 'effective' multidirectional gradients – required for multidimensional spatial encoding – are generated every subsequent 120° sample reorientation during a continuous pneumatic sample rotation about the magic-angle axis, 54.74°, with respect to the $G_z$. This rotation aligns each of the three orthogonal sample body-frame directions with $G_z$. In other words, with the constant $G_z$, at each third of the rotor period ($T_r/3 \equiv 120°$ sample rotation) three orthogonal effective gradients $G_i$ ($i = x, y, z$) are generated allowing for spatial encoding for each spatial direction with a uniform gradient magnitude. The encoding can be carried out by a standard MAS experiment with proper rotor-synchronization pulses (Fig. 1A) based on a magic-angle turning experiment [9]. Due to the simplicity of the experiment, and its ability of accessing large field gradient (up to 100 T/m) from the stray-field, this STRAFI–MAS imaging technique could be an important application to material science. After STRAFI–MAS was first demonstrated with $^1$H 2D projection spin density images [8], we further extended toward to 2D and 3D imaging of biological and inorganic solid materials with various observable nuclei: $^{29}$Si, $^{23}$Na and $^{27}$Al [10]. In this communication, we explore the possibility of contrast STRAFI–MAS – $T_1$- and $T_2$-weighted, and triple-quantum filtered imaging – on various phantoms.

## 2. Results and discussion

The dependence of $T_1$ and $T_2$ to an image spin-echo intensity ($I$) can be simplified to $I \propto (1 - \exp(-TR/T_1))\cdot\exp(-TE/T_2)$, where TR and TE are the repetition and echo time in the experiment, respectively [2]. This indicates that short $T_1$ increases the echo intensity, while short $T_2$ reduces the intensity. Thus, adjustments of TR and TE values in the STRAFI–MAS experiment could result in contrast $T_1$- and $T_2$-weighted image, respectively. For example, the

* Corresponding author. Address: CEA Saclay, DSM/IRAMIS/SIS2M/LSDRM, F-91191, Gif-sur-Yvette Cedex, France. Fax: +33 1 69 08 98 06/66 40.
*E-mail addresses:* dimitrios.sakellariou@cea.fr, dsakellariou@cea.fr (D. Sakellariou).

1090-7807/$ - see front matter © 2010 Elsevier Inc. All rights reserved.
doi:10.1016/j.jmr.2010.07.002

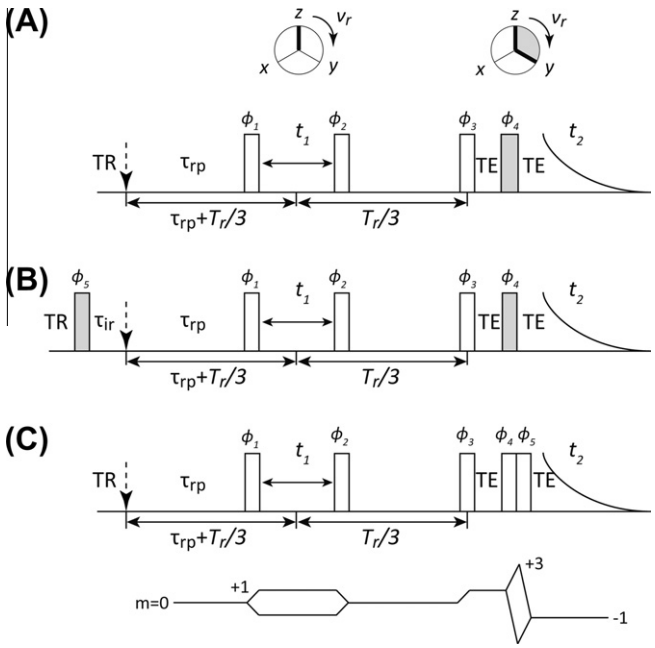


**Fig. 1.** STRAFI–MAS pulse sequence schemes. (A) Standard STRAFI–MAS for a 2D density image. (B) Inversion-recovery STRAFI–MAS for a 2D $T_1$-weighted image. (C) Triple-quantum filtered STRAFI–MAS with a coherence pathway shown below. The insert circles indicate the sample rotational phase ($x$, $y$, $z$) and $\nu_r$ is a MAS frequency. The solid grey bar represents the 180° pulse, whereas the open bar represents the 90° pulse. TR = repetition time; TE = echo time; $T_r$ = rotor period; the rotor projection delay ($\tau_{rp}$) is a experimental parameter for the rotor projection angle ($\theta_{rp}$), $\tau_{rp} = (1/\nu_r) \times (\theta_{rp}/360°)$. Phase-cycling scheme for $\phi_n$: (A and B) $\phi_1$ = [0 180]°; $\phi_2$ = [0 0 180 180]°; $\phi_3$ = [0 0 0 0 90 90 90 90 180 180 180 180 270 270 270 270]°; $\phi_4$ and $\phi_5$ = [0]°; $\phi_{rec}$ = [0 180 180 0 270 90 90 270 180 0 0 180 90 270 270 90]°; (C) $\phi_1$ = [0 180]°; $\phi_2$ = [0 0 180 180]°; $\phi_3$ and $\phi_4$ = [0 0 0 0 60 60 60 60 120 120 120 120 180 180 180 180 240 240 240 240 300 300 300 300]°; $\phi_5$ = [0]°; $\phi_{rec}$ = [0 180 180 0 180 0 0 180]°.

$T_1$-weighted $^1$H projection image of an agarose gel with $CuSO_4$ shown in Fig. 2A is carried out with a short TR of 0.5 s, which is efficient for the $^1$H spin with short $T_1$ (proton close to $Cu^{2+}$) and not with long $T_1$ (proton far from $Cu^{2+}$). The resultant pixel resolution is about 24 μm × 382 μm. The image corresponds well with the phantom and its dimensions. The phantom composes of an agarose gel inside a 4-mm MAS rotor, with the injection of ~5 μl diluted $CuSO_4$ solution in the mid section using a thin syringe. The phantom's dimensions are approximately 2.9 mm in width by 7.0 mm in length. Due to the paramagnetic effect from the $Cu^{2+}$ ions (as a $T_1$ contrast agent) on the neighboring protons – shortening the $T_1$ and enhancing the contrast – the image reveals a clear long narrow pathway (parallel to the wall) at the centre. This is caused by the needle component of a syringe during the injection of $CuSO_4$ solution. Based on the image, the diameter of the needle pathway is about 350 μm, which is in good agreement with the actual needle's diameter, 390 μm. Furthermore, the image also reveals a large and high contrast area in the mid section of the agarose gel; this is evidently the $CuSO_4$ injection spot (hot spot), where a high population of close proximity protons have been affected (shortening $T_1$) by the $Cu^{2+}$ ions, and resulted in a $T_1$ contrast enhancement.

The series of $^1$H 2D images in Fig. 2 B(i-xi) reveal the permeation of $Cu^{2+}$ ions from the hot spot inside the dense agarose gel as a function of subsequent experiments – each with 17 min acquisition time. These images are acquired subsequently with identical experimental conditions. The NMR signals are normalized to the same base level intensity for image comparison. The images evidently exhibit the permeation of $Cu^{2+}$ ions. The area with the same intensity (indicated by the dashed contour line) increases as a function of subsequent images (i.e. time); this is attributed to the fact that the copper solution diffuses from the hot spot to the bottom of the rotor. Moreover, the signal intensity at the hot spot also increases and slowly expands (Fig. 2 B-vi to -xi), this is because the $Cu^{2+}$ ion cluster has slowly scattered at the hot spot and increased the number of affected protons, thus, increased the intensity. Fig. 2 illustrates a potential application of a spatially resolved permeation/diffusion study in materials, especially in opaque materials, which are difficult to characterize with optical imaging techniques.

So far, the above $T_1$-weighted images were acquired by simply setting the experimental values of the TR parameter in such a way that longitudinal relaxation is not efficient for spins with long $T_1$ (agarose gel); however this only minimizes the intensity but cannot completely filter out the unwanted signal. By implementing an inversion recovery 180° pulse and a delay ($\tau_{ir}$) prior to the imaging pulses (Fig. 1B), it is possible to selectively separate and filter the spin of choose, if the difference in $T_1$ is large [2,3]. This is done by setting the encoding after the unwanted spin magnetization reaches to null during the $\tau_{ir}$ period. To demonstrate this, we carried out the experiment on a custom-made phantom with two volume chambers in a 4-mm rotor, separated by a Kel-F insert (2.9 mm × 2.9 mm). The bottom chamber contains a dilute $CuSO_4$ solution (short $T_1$), whereas the top chamber consists of dense agarose gel (long $T_1$). Fig. 3A displays two $T_1$-weighted images with different $\tau_{ir}$ delays, 22 and 200 ms. At 22 ms the proton signal for $CuSO_4$ solution is suppressed but retained the signal for the gel, and *vice versa* at 200 ms. It is interesting to notice that both the proton density and $T_1$-weighted images reveal a vortex (high intensity along the edges and low in the middle), with an estimate diameter of about 800 μm, in the $CuSO_4$ solution caused by the sample MAS rotation. The $T_2$-weighted image can be acquired by simply setting the TE (Fig. 1A), in such a way that it suppresses the proton with shorter $T_2$. Fig. 3A shows a $T_2$-weighted image of the same phantom as above, where the $T_2$ is slightly shorter for the $CuSO_4$ solution than that for the gel. The $T_2$-weighted image is carried out with a TE of seven rotor-synchronized periods (14 ms) allowing to filter out the signals corresponding to the $CuSO_4$ solution. The visible distortion around the edges is due to the combination of the continuous sample rotation, the inherently weak signal from $T_2$ relaxation, and the non-refocusable broadening from the molecular diffusion in the agarose gel.

Triple-quantum filtered (TQF) is also commonly adopted in contrast $^{23}$Na MRI for distinguishing $Na^+$ ions in different media; sodium in the extra- and intra-cellular of brain tissue [11], or sodium in the articular cartilages [12]. $^{23}$Na TQF imaging is targeting the slowly tumbling sodium nuclei, those with $\tau_c\omega_o \geqslant 1$, where $\tau_c$ is the molecular rotational correlation time and $\omega_o$ is the Larmor frequency. Under this condition, the $^{23}$Na nucleus experiences a nonzero averaging of the electric field gradient generated by the $^{23}$Na electronic distribution, inducing a quadrupolar coupling which allows for spin filtration of multiple-quantum coherence through rf-pulses [2,3]. $^{23}$Na TQF is a straightforward implementation in the STRAFI–MAS experiment, it simply replaces the 180° echo-pulse with two consecutive 90° pulses to allow a phase-cycling scheme, in such a way that only the triple-quantum ($p = \pm 3$) coherent magnetization contributes to the observed signal. A simple phase-cycling scheme can be constructed of a 6-step (i.e. 60°) phase-cycle for the two TQF pulses [13], resulting in an overall 24-step phase-cycling (in Fig. 1C caption). If spurious (unwanted) signals appear in the image because of the insufficient dephasing during $T_1$, it may be able to filter with an Exorcycle scheme [14] in the TQF pulses with 120° phase shifts [15]. Similar to the previous $T_1$ and $T_2$-weighted experiments, the $^{23}$Na TQF experiment is carried out on a phantom with two chambers in a 4-mm rotor. The bottom chamber consists of 300 mM NaCl in water solution, while the top chamber contains of ~5% w/v agarose gel in 300 mM NaCl solution. Fig. 3B shows the $^{23}$Na TQF image, with a

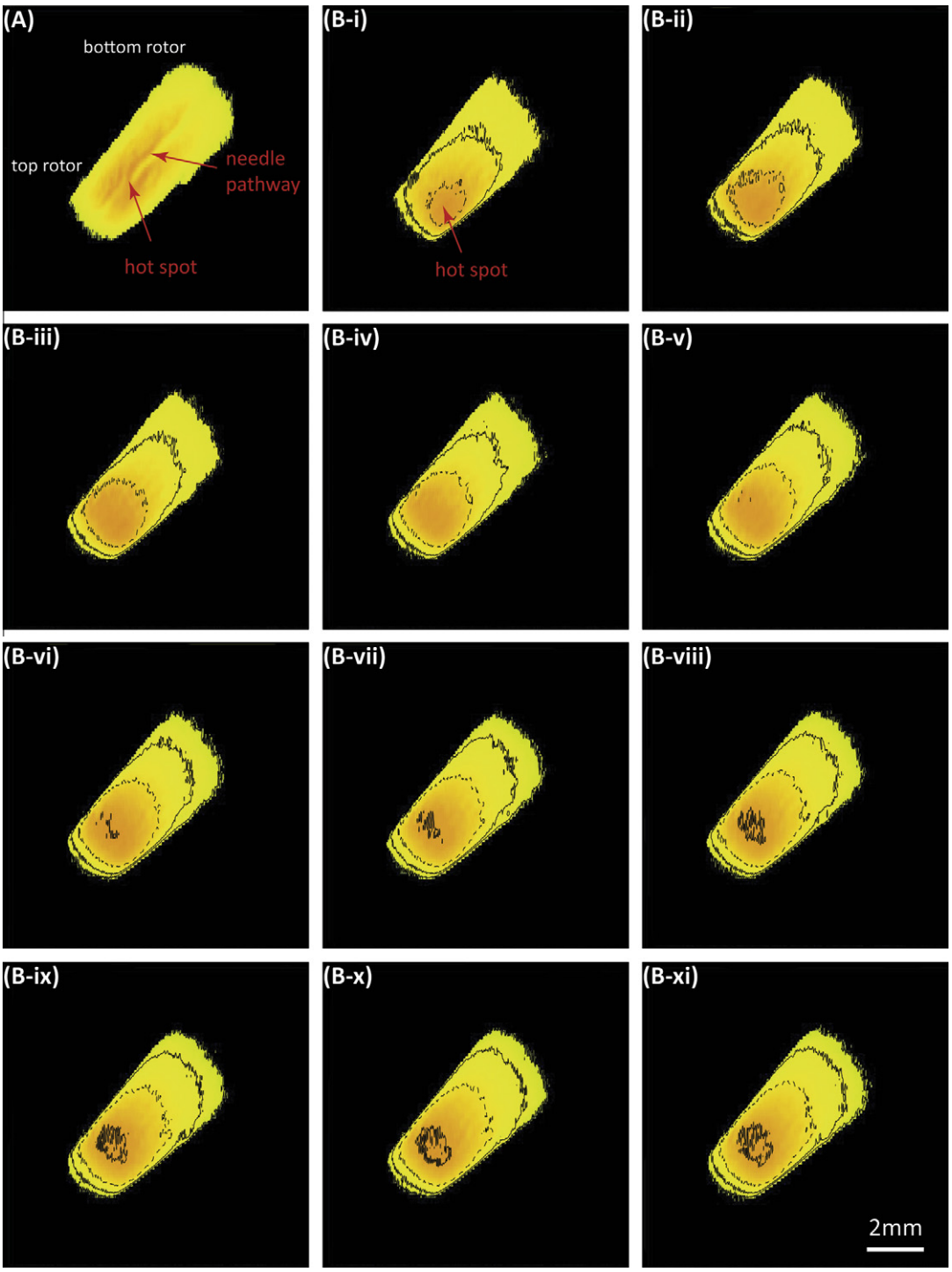


**Fig. 2.** $T_1$-weighted (with TR of 0.5 s) $^1$H images of a phantom composed of a dense agarose gel (~10% w/v of water) with an injection of ~5 μl diluted $CuSO_4$(aq). The hot spot is the area of injection. (A) Image shows the hot spot at the mid section, and reveals a needle pathway. (B-i to -xi) Snapshot images of the $Cu^{2+}$ ion permeation through the agarose gel. Images were acquired subsequently, each with an acquisition time of 17 min. All images were acquired with Fig. 1A with a short TE of 5 μs to minimize image distortion [10]. The dashed contour line represents the same intensity level allowing for visual comparison. A 2 mm spatial scale is indicated by a horizontal bar.

resolution of about 36 μm × 579 μm, has successfully filtered out the mobile $Na^+$ ion (NaCl solution) and retained the immobile $Na^+$ ions (gel) through the TQF pulses (with rf-amplitude of 114 kHz). The $^{23}$Na TQF image shown here has a modest signal-to-noise ratio (SNR ~11 of about 2 h experiment) for a phantom with 300 mM sodium concentration, which is comparable to the sodium content found in some bio tissues, such as cartilages [12]. Moreover, the feasibility of $^{23}$Na TQF imaging has been demonstrated on bovine cartilages [16], on *in vivo* human knee [17], and on a live mussel [18]. Thus, $^{23}$Na TQF STRAFI–MAS performed here could be a potential applicable for biological materials and other solid materials.

As mentioned in the previous studies [8,10], the image distortion arising from STRAFI–MAS is mainly attributed by the constant sample MAS rotation. This induces the imperfection of the effective gradient orientations (i.e. sample orientation with the static $G_z$)

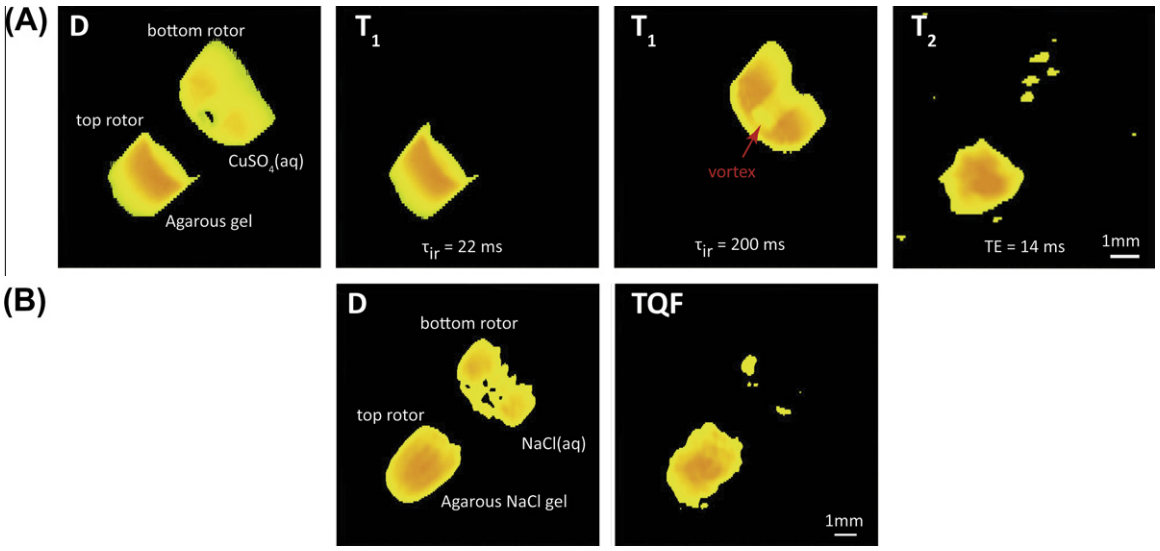


**Fig. 3.** (A) A comparison between density, $T_1$-weighted and $T_2$-weighted $^1$H images. The phantom is made out of two chambers in a 4-mm rotor, one with agarose gel and the other with diluted $CuSO_4$ solution. The $^1$H density image was acquired with Fig. 1A, whereas the $T_1$-weighted image with Fig. 1B. The $\tau_{ir}$ delay, 22 and 200 ms, corresponds to the image of gel and $CuSO_4$ solution, respectively. Both the density and $T_1$-weighted images were acquired with TE of 5 s. The $T_2$-weighted image was acquired with Fig. 1A with TE of 14 ms (7× MAS period). (B) A comparison between the density and $^{23}$Na TQF images. The phantom is a two-chambered 4-mm rotor, one with agarose NaCl gel (~5% w/v of 300 mM NaCl solution) and the other with 300 mM NaCl solution. The $^{23}$Na density image was acquired with Fig. 1A with TE of 5 s, whereas the $^{23}$Na TQF image with Fig. 1C with 2 ms TE (1× MAS period). A 1 mm spatial scale is indicated by a horizontal bar in (A) and (B).

during the evolution periods ($t_1$, $t_2$ and $t_3$), and also the spinning vibration during the encoding. We countered these issues by slow sample spinning (500 Hz) with excellent stability (less than ±1 Hz), and have shown its effectiveness of minimizing the distortion arising from the continuous sample spinning. However, slight apparent non-linear edges do appear in the acquired images. Further improvements could be carried out by a numerically correction (i.e. re-gridding of $k$-space) of the imperfect effective gradient orientations during the evolution periods ($t_1$, $t_2$ and $t_3$), or by a discrete rotation of 120° of the sample around the axis pointing at the magic-angle with respect to the static magnetic field. The latter approach is called magic-angle hopping (MAH) [19]. It has been used for high-resolution solid-state NMR spectroscopy but not yet for imaging purposes. With MAH, the sample is not under a continuous rotation, hence, the image distortions could be in principle completely eliminated. However, it requires specialized and demanding hardware. Currently, we are working on the numerical approach to correct the imperfection of the effective gradient orientations, in hope to improve the quality of the STRAFI–MAS image.

This short communication demonstrates the possibility of acquiring contrast MR images using a simple and effective STRAFI–MAS approach, where no traditional imaging equipments are necessary. With the current advancements in both NMR and MRI, STRAFI–MAS is expected to be further improved and developed (i.e. eliminating image distortions, or accessing larger gradient for ultra high spatial resolution). We anticipate that STRAFI–MAS would becomes a promising imaging technique, especially for solid materials [20].

## 3. Experimental methods

STRAFI–MAS measurements were performed on a 7.05 T wide-bore (89 mm) nonshielded Oxford magnet with an Avance 300 console. Images were acquired with a Bruker 4-mm HXY CPMAS probe with a MAS frequency of 500 Hz and a stability of less than 1 Hz. This slow and stable spinning was achieved by using a custom-made turbineless Kel-F rotor cap [21]. It is to note that such slow and stable spinning minimized image distortions resulting from the rotor vibration and the imperfect gradient orientation during the $t_1$ and $t_2$ encodings. The probe's magic-angle, 54.74°, was carefully calibrated with $^{89}$Br NMR of KBr. The field gradient ($G_z$) was achieved by positioning the MAS probe at an offset from its standard position inside the bore of an NMR magnet. Positioning along the bore ensured the probe is perfectly aligned with the $z$-directional field. No additional gradient systems were necessary. The $^1$H images were acquired with a probe offset of 7.4 cm, which provided a $G_z$ of ~0.24 T/m. The operating frequency was 299.40 MHz. The pulse-width for the 90° pulse was set to 2.0 μs, which corresponds to a $^1$H rf-amplitude of 125 kHz. TR was set to 0.5 s. The 2D image was collected with 2048 and 128 complex data points in both $F_2$ and $F_1$ dimensions with a spectral-width of 250,000 Hz. For $^{23}$Na image, the probe offset was set to 6.7 cm, resulting in a $G_z$ of ~0.12 T/m. The image was carried out at 79.20 MHz Larmor frequency with a 90° pulse-width of 2.2 μs ($^{23}$Na rf-amplitude of 114 kHz), and TR of 100 ms. 1024 and 64 complex points were collected in both $F_2$ and $F_1$ dimensions with a spectral-width of 25,000 Hz. Since all phantoms consist of high degrees of cylindrical symmetry, the rotor projection delay ($\tau_{rp}$) is set to zero in all $^1$H and $^{23}$Na acquisitions. $^1$H and $^{23}$Na 2D images were recorded with States phase-cycling [22] and processed with an exponential apodization of 200 Hz, on the time-domain $t_1$ and $t_2$ data to improve the signal-to-noise. Zero-filling up to 256 points in $F_1$ and 2048 points in $F_2$ were applied to improve the pixel definition quality. Further experimental details are provided in the figure captions.

## Acknowledgments

This work is supported by European Research Council under the European Community's Seventh Framework Programme (FP7/2007–2013): ERC Grant Agreement #205119.

## References

[1] G.T. Herman, Fundamentals of Computerized Tomography: Image Reconstruction from Projection, second ed., Springer, 2009.

[2] P.T. Callaghan, Principles of Nuclear Magnetic Resonance Microscopy, Clarendon Press, Oxford, 1991.
[3] B. Blümich, NMR Imaging of Materials, Clarendon Press, Oxford, 2000.
[4] R.S.- Bindman, J. Lipson, R. Marcus, K.-P. Kim, M. Mahesh, R. Gould, A.B. de González, D.L. Miglioretti, Radiation dose associated with common computed tomography examinations and the associated lifetime attributable risk of cancer, Arch. Intern. Med. 169 (2009) 2078–2086.
[5] E.M. Haacke, R.W. Brown, M.R. Thompson, R. Venkatesan, Magnetic Resonance Imaging: Physical Principles and Sequence Design, J. Wiley & Sons, New York, 1999.
[6] E.T. Ahrens, P.T. Narasimhan, T. Nakada, R.E. Jacobs, Small animal neuroimaging using magnetic resonance microscopy, Prog. Nucl. Magn. Reson. Spectrosc. 40 (2002) 275–306.
[7] M.I. Kettunen, K.M. Brindle, Apoptosis detection using magnetic resonance imaging and spectroscopy, Prog. Nucl. Magn. Reson. Spectrosc. 47 (2005) 175–185.
[8] J.H. Baltisberger, S. Hediger, L. Emsley, Multi-dimensional magnetic resonance imaging in a stray magnetic field, J. Magn. Reson. 172 (2005) 79–84.
[9] Z. Gan, High-resolution chemical shift and chemical shift anisotropy correlation in solids using slow magic-angle spinning, J. Am. Chem. Soc. 114 (1992) 8307–8309.
[10] A. Wong, D. Sakellariou, 2D and 3D multinuclear stray-field imaging of rotating samples with magic-angle spinning (STRAFI–MAS): from bio to inorganic materials, J. Magn. Reson. Imaging, in press.
[11] I. Hancu, F.E. Boada, G.X. Shen, Three-dimensional triple-quantum-filtered $^{23}$Na imaging of in vivo human brain, Magn. Reson. Med. 42 (1999) 1146–1154.
[12] A. Borthakur, E. Mellon, S. Niyogi, W. Witschey, J.B. Kneeland, R. Reddy, Sodium and $T_1\rho$ MRI for molecular and diagnostic imaging of articular cartilage, NMR Biomed. 19 (2006) 781–821.
[13] S. Wimperis, P. Cole, P. Styles, Triple-quantum-filtration NMR imaging of 200 mM sodium at 1.9 Tesla, J. Magn. Reson. 98 (1992) 628–636.
[14] G. Bodenhausen, R. Freeman, D.L. Turner, Suppression of artifacts in two-dimensional J spectroscopy, J. Magn. Reson. 27 (1977) 511–514.
[15] G. Bodenhausen, H. Kogler, R.R. Ernst, Selection of coherence-transfer pathways in NMR pulse experiments, J. Magn. Reson. 58 (1984) 370–388.
[16] R. Reddy, E.K. Insko, J.S. Leigh, Triple quantum sodium imaging of articular cartilage, Magn. Reson. Med. 38 (1997) 279–284.
[17] A. Borthakur, I. Hancu, F.E. Boada, G.X. Shen, E.M. Shapiro, R. Reddy, *In vivo* triple quantum filtered twisted projection sodium MRI of human articular cartilage, J. Magn. Reson. 141 (1999) 286–290.
[18] R.K.- Harper, P. Styles, S. Wimperis, Three-dimensional triple-quantum filtration $^{23}$Na NMR imaging, J. Magn. Reson. B 108 (1995) 280–284.
[19] A.D. Bax, N.M. Szeverenyi, G.E. Maciel, Correlation of isotropic shifts and chemical shift anisotropies by two-dimensional Fourier-transform magic-angle hopping NMR spectroscopy, J. Magn. Reson. 52 (1983) 147–152.
[20] A.T. Watson, C.T.P. Chang, Characterizing porous media with NMR methods, Prog. Nucl. Magn. Reson. Spectrosc. 31 (1997) 343–386.
[21] A. Wong, P.M. Aguiar, D. Sakellariou, Slow magic-angle coil spinning: a high-sensitivity and high-resolution NMR strategy for microscopic biological specimens, Magn. Reson. Med. 63 (2010) 269–274.
[22] D.J. States, R.A. Haberkorn, D.J. Ruben, A two-dimensional nuclear overhauser experiment with pure absorption phase in four quadrants, J. Magn. Reson. 24 (1982) 286–292.